Article:

Hamdan, S., Wigglesworth, M.J., Muscetta, M. et al. (2025) Unravelling the photoactivity of metal-loaded TiO2 for hydrogen production: Insights from a combined experimental and computational analysis. International Journal of Hydrogen Energy, 118. pp. 394-406. ISSN: 0360-3199

https://doi.org/10.1016/j.ijhydene.2025.03.184

International Journal of Hydrogen Energy 118 (2025) 394–406

Contents lists available at ScienceDirect

International Journal of Hydrogen Energy

journal homepage: www.elsevier.com/locate/he

Unravelling the photoactivity of metal-loaded TiO_2 for hydrogen production: Insights from a combined experimental and computational analysis

Sarah Hamdan [a,b,1], Matthew J. Wigglesworth [c,1], Marica Muscetta [d,*], Ruiman Ma [c], Mohamed I. Helal [e], Natalia Martsinovich [f], Giovanni Palmisano [a,b], Sergio Vernuccio [g,**]

[a] Department of Chemical and Petroleum Engineering, Khalifa University, P.O. Box 127788, Abu Dhabi, 127788, United Arab Emirates
[b] Research and Innovation Center on CO_2 and Hydrogen, Khalifa University of Science and Technology, P.O. Box 127788, Abu Dhabi, United Arab Emirates
[c] School of Chemical, Materials and Biological Engineering, University of Sheffield, Sheffield, United Kingdom
[d] Department of Chemical, Materials and Industrial Production Engineering, University of Naples Federico II, P.le Tecchio 80, Naples, 80125, Italy
[e] CORE Lab Specialist, Electron Microscopy Core Labs, Khalifa University, Abu Dhabi, 127788, United Arab Emirates
[f] School of Mathematical and Physical Sciences, University of Sheffield, Sheffield, United Kingdom
[g] School of Chemistry and Chemical Engineering, University of Southampton, Southampton, United Kingdom

ARTICLE INFO

Handling Editor: Søren Juhl Andreasen

ABSTRACT

Despite being the most employed material for photocatalytic hydrogen generation, TiO_2 suffers limitations such as a high rate of electron-hole recombination and poor light absorption in the visible spectrum. Among the various strategies developed to overcome these drawbacks, combining TiO_2 with a metal co-catalyst emerged as one of the most promising. In this study, we integrated experimental findings, advanced characterization techniques, and computational methods to shed light on how different noble metals influence the enhancement of the photocatalytic activity of TiO_2. Among the tested noble metal co-catalysts, the hydrogen production rate under UV and visible light irradiation followed the trend $Pt > Au \approx Pd > Ag >$ bare TiO_2, with Pt-decorated TiO_2 exhibiting a hydrogen production rate of 28 mmol/h g. The noble metals were found to significantly suppress the electron-hole recombination rate compared to bare TiO_2. Upon photodeposition, Pd and Pt formed the smallest nanoparticles with average sizes of 13.4 nm and 4.1 nm, respectively. Computational analyses were conducted to rationalize the difference in nanoparticle sizes by analyzing the binding and cohesive energies of the metal clusters on the TiO_2 surface. Additionally, calculations demonstrated the strong interaction of Pt, Au, and Pd nanoclusters with adsorbed hydrogen, with Pt achieving the closest-to-zero Gibbs free energy of hydrogen adsorption and displaying the most polar interaction with hydrogen. These findings align closely with the observed hydrogen production rates, where UV/Vis-driven hydrogen production is governed by the coupling of hydrogen radicals on the co-catalyst surface, while visible-light-driven production is limited by charge carrier lifetimes.

1. Introduction

Due to the imminent depletion of conventional energy sources, photocatalytic production of hydrogen is a critical challenge in the pursuit of clean and renewable energy [1–3]. Currently, the application of solar hydrogen production from renewable resources is limited, with the primary method being water electrolysis [4,5]. However, among the techniques for hydrogen production, sacrificial photoreforming stands out as one of the most promising, attracting significant global research interests [6,7].

Titanium (IV) oxide (TiO_2) is a semiconductor recognized for its excellent photostability and highest sustained photocatalytic activity in these processes. However, one of the main limitations of TiO_2 is its high rate of photogenerated electron-hole pair recombination, which

---

* Corresponding author.
** Corresponding author.
E-mail addresses: marica.muscetta@unina.it (M. Muscetta), s.vernuccio@soton.ac.uk (S. Vernuccio).

[1] the authors contributed equally to the manuscript.

https://doi.org/10.1016/j.ijhydene.2025.03.184
Received 19 January 2025; Received in revised form 10 March 2025; Accepted 11 March 2025

significantly reduces its photocatalytic efficiency. Indeed, high recombination rates, with a charge carrier lifespan of around 30 ns, result in insufficient time for further chemical reactions to occur. Another disadvantage of TiO_2 is its wide band gap (3.0–3.2 eV), which limits its light absorption primarily to the UV range [7]. Since UV irradiation accounts for only 4 % of the solar spectrum, a major challenge for TiO_2-based photocatalytic processes is the limited utilization of solar energy. To address these drawbacks, previous studies have aimed to enhance the semiconductor activity by reducing the electron-hole recombination rate and extending the light adsorption to the visible range [8,9], typically through the combination of the semiconductor with a co-catalyst [10,11]. Among the various strategies employed, loading TiO_2 with noble or non-noble metals is one of the most promising approaches [12–14]. Several reviews have been published that discuss the behaviour of metals on the catalyst surface, offering possible explanations for the different observed activity [15,16]. For instance, Kumaravel et al. [17] reported that metal dopants can enhance the charge carrier separation and the spectral response of TiO_2 through various mechanisms, including the surface plasmon resonance (SPR) effect, the electron trap mechanism, the generation of gap states from interaction with TiO_2 valence band (VB) states, and the introduction of new energy levels. Defect engineering is a powerful technique for tuning the properties of a material to optimize its performance for specific functions [18]. It has been suggested that doping a photocatalyst with a metal of higher work function can enhance charge separation, thereby improving the photocatalyst's efficiency [19]. The role of metal loading is to primarily enhance charge carrier separation in the photocatalyst. This is achieved by introducing metal traps, which extend the lifetimes of these catalytically active charge carriers, resulting in more successful redox reactions on the surface. The formation of the Schottky barrier upon metal deposition on the semiconductor surface further promotes charge separation, by facilitating electron transfer from the bulk semiconductor to the metal sites.

From a theoretical perspective, DFT studies have proven to be powerful tools to select and design photocatalysts for efficient hydrogen production [20], as well as interpreting experimental results. However, these calculations require certain assumptions. The process of interest is typically studied on a small fragment of the photocatalyst's surface, assuming it has a periodic structure. For example, Assadi et al. conducted a theoretical study to explain the enhancement of anatase photoactivity through copper doping [21]. According to their computational results, enhancement was attributed to electronic interactions, facilitated by charge transfer and the formation of inter-bandgap states. Wen et al. utilized DFT to explore the photocatalytic behaviour of iron-doped photocatalysts [22]. That study revealed that the Fe^{3+} ions on the TiO_2 surface can provide an intermediate interfacial transfer pathway for the photogenerated charges, thus increasing the photocatalytic activity of TiO_2. However, purely computational studies should be treated with extreme caution [23] and their combination with appropriate characterization techniques is crucial to fully understand how metals modify the photocatalytic properties of TiO_2 [7,24]. For this purpose, some authors have reported the possibility of determining the correlations between the material properties and the photocatalytic performance based on theoretical calculations and/or systematic characterizations [25]. However, despite the extensive body of research on TiO_2-based photocatalysts, the primary factors influencing the variation of photoactivity depending on the metal co-catalyst remain unclear [12,17,26]. In this study, we propose an innovative synergistic approach that integrates state-of-the-art characterization techniques with advanced computational methodologies. This approach systematically investigates the role of metal co-catalysts in enhancing the photoactivity of TiO_2 for hydrogen production. By integrating experimental and theoretical insights, this framework offers a comprehensive model for designing photocatalytic systems, leveraging the interplay between semiconductors and transition metals.

2. Materials and methods

2.1. Materials

TiO_2 (anatase) nanopowder (<25 nm particle size, 99.7 % trace metal basis), palladium (II) chloride ($PdCl_2$, ≥99.9 %), silver nitrate ($AgNO_3$, ACS reagent, ≥99.0 %), gold (III) chloride trihydrate ($AuCl_3 \bullet 3H_2O$, ≥99.9 % trace metals basis), chloroplatinic acid hexahydrate ($H_2PtCl_6 \bullet 6H_2O$, ACS reagent, ≥37.50 % Pt basis) and methanol (99 %) were purchased from Sigma Aldrich. All reagents were used as received. Doubly glass-distilled water was used throughout this study.

2.2. Photocatalysis experiments

Photocatalytic experiments were conducted batchwise in an annular quartz batch reactor, placed in a quartz lamp jacket and fitted with high-pressure mercury vapour lamps (Nominal power P = 400 W) and a daylight lamp (Nominal power P = 150 W) both by Photochemical Reactors Ltd, as described in previous reports [27]. The effective irradiances of the medium pressure mercury vapour lamp were $1.17 \bullet 10^{-6}$ E s^{-1} (302 nm), $3.19 \bullet 10^{-6}$ E s^{-1} (313 nm), $3.41 \bullet 10^{-7}$ E s^{-1} (334 nm), $6.97 \bullet 10^{-6}$ E s^{-1} (366 nm) in the UV range, and $3.04 \cdot 10^{-5}$ E s^{-1} (406 nm), and $6.62 \cdot 10^{-5}$ E s^{-1} (436 nm) in the visible range. The effective irradiances of the daylight lamp were $2.84 \bullet 10^{-5}$ E s^{-1} (420 nm), $5.63 \bullet 10^{-5}$ E s^{-1} (535 nm), $8.14 \bullet 10^{-5}$ E s^{-1} (585 nm), and $4.28 \bullet 10^{-5}$ E s^{-1} (670 nm), all in the visible range. In a typical experimental run, 150 mg of TiO_2 nano powder was suspended in a 2.5 M methanol aqueous solution (total volume = 0.30 L) at natural pH. To prevent dissolved oxygen from reacting with photogenerated electrons, nitrogen gas was bubbled through the solution for 40 min before the photocatalytic experiments at a flow rate of 0.30 L min^{-1}. The temperature of the system, controlled with a thermostat, was fixed to 25 °C. The composite materials were prepared through in-situ photodeposition of the metals onto the anatase surface, by adding selected concentrations of metal ions ($Metal/TiO_2$ = 7.5 % mol) to the mixture in the form of salts. Specifically, depending on the metal, a selected amount of metallic salts was employed. To assess the activity under visible light irradiation, the visible lamp was used, after photodeposition of the metals in the presence of the UV lamp. In some cases, the photocatalyst was recovered at the end of the run, as previously described [28].

To evaluate the hydrogen production rate, gaseous samples were periodically collected using Tedlar gas sampling bags (1 L) at different reaction times. These samples were analysed using a gas chromatograph (Trace 1310), equipped with a HS-Q column (2 m, 60/80 mesh) and a TCD detector using argon as carried gas. The pH of the solution was monitored through an Orion 420 p pH-meter (Thermo).

2.3. Characterization techniques

A variety of advanced characterization tools were utilized in order to examine the chemical and physical properties of the photocatalyst synthesized in this study, including X-ray Diffraction (XRD), X-ray photoelectron spectroscopy (XPS), Scanning Transmission Electron Microscopy coupled with Energy Dispersive Spectroscopy (STEM-EDX), Brunauer- Emmett-Teller (BET) analysis, UV–Vis Diffuse Reflectance Spectroscopy (UV-DRS), Electrochemical Impedance Spectroscopy (EIS), and Photoluminescence (PL).

Structural properties of the photocatalysts were analysed using Empyrean Panalytical X-ray Diffractometer in 2Q range 20°–80° angle with Cu Kα radiation (1.5406 Å) in 0.02 step size using the program reflection transmission spinner (RTS). X-ray tension was 20 kV and current was 15 mA.

A PHI VersaProbe 5000 Scanning X-ray Photoelectron Spectrometer equipped with a MgKα X-ray source (1100 eV) was used to conduct the XPS analysis. The power of the X-ray beam was 50.17 W. The analysis was conducted using a E-neutralizer (1 V) and a I-neutralizer (0.11 kV

Ar^+ ion). The samples were etched in-situ with a 3 kV Ar beam for 1 min to remove impurities from the top 20 nm layer prior to the XPS measurements. The analysis is done using Aventage software and all peaks are referenced to C 1s.

Transmission electron microscopy (TEM) and STEM-EDX analyses were carried out at 200 kV utilizing Tecnai G2 transmission electron microscopes. First, the powder was suspended in water and subjected to ultrasonic treatment. Three microliters of the suspension were placed twice in a row on a Tedpella-provided 400-mesh Cu grid. After that, water was evaporated at ambient temperature. To compute the particle size distribution, ImageJ was utilized.

Using N_2 as the adsorbate, the Quantachrome NOVA 2000e surface area and pore size analyzer and the Anton Paar Nova 800 physisorption analyzer were used to assess the adsorption/desorption isotherms of the catalysts. The samples were degassed under vacuum for 6 h at 250 °C before analysis. The multipoint BET technique was applied in the low-pressure regime (desorption points $P/P_0 = 0$–0.35) to obtain the specific surface area. The pore size distribution was calculated by fitting the adsorption curve over the whole pressure range to the Barrett-Joyner-Halenda (BJH) model.

The optical properties of the investigated photocatalyst samples were assessed using Shimadzu Europe-UV-2600-room temperature photoluminescence (PL) spectra, which were obtained with a PerkinElmer LS-55 at $\lambda_{ex} = 400$ nm, 4.5 nm emission and excitation slits, and a 100 nm/min scan speed.

The UV–vis diffuse reflectance spectra (DRS) were obtained using a UV–vis spectrophotometer (Shimadzu UV-2600) equipped with an integrating sphere attachment and $BaSO_4$ as the reflectance standard, in addition to the photoluminescence. The UV–vis DRS were recorded in the 250–750 nm range.

A PGSTAT302 N Potentiostat connected to a three-electrode system was used for measurements of electrochemical impedance spectroscopy (EIS) of the as-obtained samples. The EIS was performed in dark and under UV (370 nm) illumination in the frequency range of 0.1 Hz–10 kHz with an applied potential of 0.9 V vs NHE. The photoelectrochemical measurement was carried out using a Metrohm Autolab with the sample deposited on a fluorine doped tin oxide (FTO) as the working electrode, platinum electrode as the counter electrode, and a saturated silver chloride (Ag/AgCl) electrode as the reference electrode. A 0.5 M Na_2SO_4 electrolyte solution (pH 5.6) was used for the analysis. The working electrode was prepared by suspending 4 mg of the sample in 4 mL of 2-propanol. Followed by 15 min of ultrasonic treatment. The FTO glass surface (1 cm × 2.5 cm part) was covered with 10 μL of each suspension using a micropipette, allowing it to dry completely before applying additional layers. This deposition was repeated 15 times, resulting in a total catalyst loading of 150 μg on the FTO surface.

2.4. *Computational methods*

DFT calculations were performed using the 5.4.4 version of the Vienna ab initio Simulation Package (VASP) [29,30]. The Generalised Gradient Approximation (GGA) with the Perdew-Burke-Ernzerhof functional (PBE) was employed to obtain exchange-correlation energies in all calculations [31]. The Projector Augmented Wave (PAW) method was used to describe the inner electrons [32,33]. The cutoff energy of the plane-wave basis set was set to 520 eV. Single atoms and isolated clusters were calculated in boxes 13x14x15 Å. van der Waals interactions were represented by including Grimme's DFT-D3 dispersion correction method, along with the Becke-Johnson BJ damping method for interatomic distances [34,35]. Structural optimization allowed for symmetry breaking to ensure a more accurate representation of the system. Interactions within the semiconductor material were incorporated to correct the electron self-interaction by applying the Coulomb interaction U and the electronic exchange J following Dudarev's approach of GGA + U [36]. A U value of 2 was applied to the Ti 3d orbitals as suggested by Metiu and Hu [37]. Fig. S1 displays the impact of the value of U on the Gibbs free energy of hydrogen adsorption on metal clusters on TiO_2 and confirms a consistent trend for different U values.

The lattice parameters for the anatase structure were optimised to b = 7.49 Å and c = 10.47 Å. The catalyst was modelled by a 2x2x3-extended primitive cell ($Ti_{24}O_{48}$) to mimic the bulk lattice structure. The system was periodic in two dimensions, forming a (101)-oriented anatase slab. A vacuum length of 20 Å was set in the non-periodic direction to avoid spurious interactions between neighbouring slabs. A single Gamma k-point (1 × 1 × 1) was deemed sufficient for these calculations. For the convergence criteria in all calculations, 10^{-6} eV was set for the self-consistent field and 0.01 eV/Å for the atomic forces. A conjugate-gradient optimization method was used to optimize the structures. The Vaspkit package was used to apply corrections to estimate the Gibbs free energy [38].

The photocatalysts were modelled using metal clusters (Pt_x, Au_x, Pd_x, Ag_x, with x ranging from 3 to 6) adsorbed on the anatase (101) surface. The adsorbed cluster structures were informed by earlier literature studies [39–42]. Each metal has several variations of optimised cluster configurations, with some clusters lying flat on the TiO_2 surface and others standing upright. The most stable optimised shapes of the adsorbed trimer clusters are reported in Fig. S2. These configurations prefer having at least two of the three atoms bonded to O_{2c} atoms on the semiconductor surface, indicating that this bonding may play a part in its stability.

The adsorption energy of a metal cluster on the TiO_2 surface (ΔE_{TM}) was defined by Equation (1), where E_{slab} is the energy of the relaxed pristine TiO_2, E_{TM_x} is the energy of a transition metal cluster (TM_x, where TM is Pt, Au, Pd, or Ag) in its most stable configuration, and E_{TM_x/TiO_2} is the energy of the TM_x/TiO_2 structure. The more negative the adsorption energy, the stronger the binding.

$$\Delta E_{TM} = E_{TM_x/TiO_2} - (E_{slab} + E_{TM_x}) \tag{1}$$

Cohesive energy (E_{coh}) was defined as the energy released per transition metal atom in forming the adsorbed structure TM_x/TiO_2 according to the formula:

$$E_{coh} = \frac{E_{TM_x/TiO_2} - (E_{slab} + x \cdot E_{TM_1})}{x} \tag{2}$$

where E_{TM_1} is the energy of a single isolated metal atom.

To evaluate the reactivity of each metal co-catalyst, the adsorption energy of a single hydrogen atom ΔE_H was calculated using Equation (3). $E_{H/TM_3/TiO_2}$ is the energy of the catalytic system with the hydrogen adsorbed on the TM_x cluster on anatase, and E_{H_2} is the energy of an isolated diatomic hydrogen molecule.

$$\Delta E_H = E_{H/TM_x/TiO_2} - E_{TM_x/TiO_2} - \frac{1}{2}E_{H_2} \tag{3}$$

The Gibbs free energy of hydrogen adsorption (ΔG_H) was calculated using Equation (4):

$$\Delta G_H = \Delta E_H + \Delta E_{ZPE} - T \bullet \Delta S \tag{4}$$

where ΔE_{ZPE} and ΔS are the difference in zero-point energy and the difference in entropy between adsorbed hydrogen and hydrogen molecule in the gas phase, respectively. T is the temperature of 298 K.

The charge density difference (CDD) $\Delta\rho$ was calculated based on Equation (5). $\rho_{H/TM_x/TiO_2}$ is the charge density of the entire system, ρ_H is the charge density of the adsorbed hydrogen, and ρ_{TM_x/TiO_2} is the charge density of the TM_x/TiO_2 system with no adsorbate present.

$$\Delta\rho = \rho_{H/TM_x/TiO_2} - \rho_H - \rho_{TM_x/TiO_2} \tag{5}$$

3. Results and discussion

3.1. Photocatalyst characterization

To investigate the crystalline characteristics of TiO_2 loaded with Au, Ag, Pd and Pt, X-ray diffraction (XRD) patterns were recorded as illustrated in Fig. 1. It is well reported that the anatase phase of TiO_2 exhibits major reflections at 25.5°, 38.2°, 48.2°, 54.6°, 55.2°, 63.3°, 69.4°, 70.8°, and 75.5° corresponding to (101), (004), (200), (105), (211), (204), (106), (220), and (215) planes, as referenced in JCPDS No. 21–1272 [43, 44]. Strong diffraction peaks at 25° and 48° confirm that TiO_2 used in this study is in the anatase phase. The observed XRD pattern of Ag-loaded TiO_2 sample shows unambiguously that a mixed phase of face-centered, cubic Ag and anatase has formed. Distinctive 2θ° values at 38.1°, 44.3°, 64.4° correspond to the metallic Ag in the face centered lattice at (113), (124), and (220) as well matched with JCPDS card No. 65–2871 [45]. The Pd peak observed at 40.4° for the Pd-loaded sample is assigned to the (111) plane. Because Pd nanoparticles are very small, the peaks appear to be considerably broad [46]. The face-centered cubic Au (JCPDS card No. 002–1095) and anatase TiO_2 (JCPDS card No. 21–1272) can be identified by reflections in the diffraction pattern of the Au-loaded sample. The diffraction peaks at 2θ° values of 44.7°, 62.9°, and 77.7° correspond to the Au nanoparticles' (200), (220), and (311) planes, respectively. This indicates the successful formation of metallic Au nanoparticles on the surface of TiO_2 [47]. Pt nanoparticles were detected at 2θ° angles of 39.9° and 48.3° which can be indexed as (111) and (210) reflections of metallic Pt (JCPDS No. 01–1194) [48]. Additionally, Pt nanoparticles exhibited the broadest peaks among the metals studied here, indicating a smaller particle size compared to the others [50].

The surface composition of the metal-loaded TiO_2 nanoparticles was examined using XPS. Fig. 2a illustrates the surface survey XPS spectra of bare TiO_2 and Pd-, Pt-, Ag- and Au-loaded TiO_2. Fig. 2b shows the Ti 2p spectrum of bare TiO_2 nanoparticles, exhibiting peaks at 458.1 eV and 463.6 eV, corresponding to Ti^{4+} in TiO_2 and a peak at 460.4 corresponding to $Ti^{3+.}$ These results confirm the full oxidation of titanium. The nearly symmetric peaks and the binding energy difference of approximately 6 eV are consistent with typical values reported for TiO_2 [49]. Furthermore, the high-resolution spectrum of O 1s of the samples was deconvoluted into three peaks at 530.6, 532.7 eV, and 534.1 eV as shown in Fig. 2c. The peaks indicate bridging oxygen, terminal hydroxyl groups and the last peak at 534.1 eV corresponds to physically adsorbed water (H_2O) [50]. Fig. 2d displays the Pd 3d spectrum. Pd $3d_{5/2}$ and $3d_{3/2}$ states are located at 334.7 and 340.0 eV, and the peaks located at 335.7 and 340.8 eV correlate to the Pd^{2+} $3d_{5/2}$ and $3d_{3/2}$ states. Furthermore, the presence of Pd^{2+} peaks arise from the partial oxidation of the palladium surface. This mainly arises from the relatively small size of Pd nanoparticles [51]. In the case of Pt loaded TiO_2, it is observed in Fig. 2e the spectra for Pt 4f, revealing peaks corresponding to metallic Pt^0 as well as a higher oxidation state, which can be attributed to Pt^{2+} and Pt^{4+}.

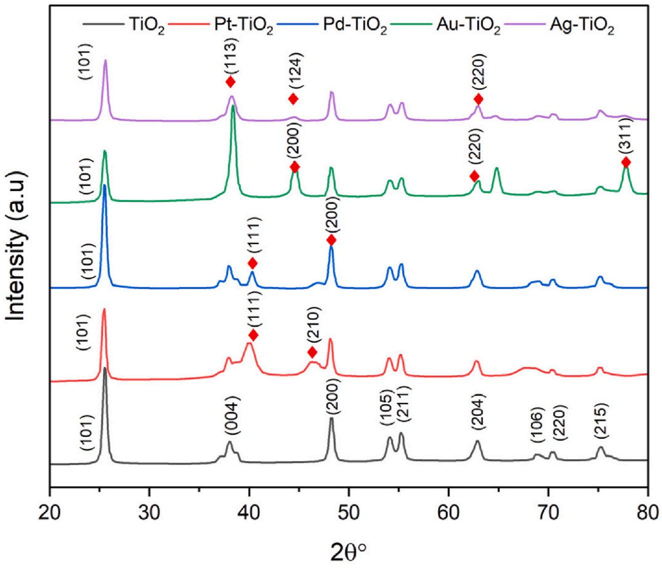

Fig. 1. X-ray diffraction peaks of metal-loaded TiO_2.

The stoichiometry of the PtO_x species produced from the reaction between small Pt particles and oxygen is dependent on the size of the particles. In agreement with Wang et al. [51], the x value varies from 1 to 2 with the decrease in particle size, specifically below 2 nm. Given a range of Pt particle sizes, it can be expected that the smallest Pt particles will oxidize to form PtO_2, whereas the larger particles will produce PtO species. A PtO oxide layer may also form on the surface of the metallic Pt particles. Consequently, the detected Pt^{2+} oxidized species might be present either as a PtO coating on the Pt^0 particles or as oxidized PtO particles. Zhang et al. [52] proposed that Pt^0 sites can possibly be oxidized to Pt^{2+} species, which in turn substitutes for Ti^{4+} ions in the TiO_2 lattice [53]. Furthermore, The Pt^{4+} state suggests that there may be a strong interaction between platinum and TiO_2, possibly leading to the formation of Pt–*O*–Ti bonds, which stabilize the oxidized platinum state [54]. However, the oxidation of metallic Pd and Pt is reversible, as these can be reduced back to their metallic forms under the anaerobic conditions employed during hydrogen evolution reactions. This reversible behaviour has been documented in previous literature. For instance, Kumaravel et al. [55] reported that under anaerobic conditions, hydrogen can act as a reducing agent to restore oxidized noble metals to their metallic states. Therefore, Pt and Pd in this study got reduced from the oxidized states of Pd and Pt to their metallic states. The Ag $3d_{5/2}$ and Ag $3d_{3/2}$ peaks (Fig. 2f) are attributed to binding energies of 374.2 and 368.2 eV, respectively. The 6.0 eV separation between the peaks suggests the successful formation of metallic Ag, confirming that the in-situ reduction of silver has taken place [56]. Moreover, peaks of Ag^+ appeared at binding energies of 367 and 373 eV, respectively. The Ag^+ peak indicates the presence of silver in an oxidized state, likely Ag(I). This could be due to the interaction of silver with the TiO_2. The oxidation of silver can occur in the presence of oxygen or hydroxyl groups from TiO_2, leading to the formation of Ag^+ (e.g., Ag_2O or $AgTiO_3$ species) [57]. Additionally, as illustrated in Fig. 2g, the XPS spectra of Au shows the occurrence of Au $4f_{5/2}$ and Au $4f_{7/2}$ doublet with binding energies of 93.3 and 86.9 eV respectively, which are characteristic for Au in the Au^0 state [49]. Notably, Au–TiO_2 showed distinct peaks at 84.0 and 87.6 eV (Fig. 2g), corresponding to $Au^{\delta+}$species, probably because $Au^{\delta+}$ can be stabilized on the surface of TiO_2 nanoparticles. It is speculated that such $Au^{\delta+}$ species may be incorporated into a part of the peripheral sites of the Au clusters on the TiO_2 surface, resulting in a strong interaction between the Au clusters and the TiO_2 NPs, thus avoiding sintering during the reaction [58].

Furthermore, XPS analysis of Ti 2p and O 1s are represented in Figs. S5 and S6, respectively. In Fig. S5 (Ti 2p), two distinct peaks at 459.4 and 465.1 eV correspond to the Ti $2p_{3/2}$ and Ti $2p_{1/2}$ spin–orbit components, characteristic of the Ti^{4+} oxidation state [59]. However, a slight shift of 0.12 and 0.15 eV is observed from TiO_2 (458.94 eV) to Pd–TiO_2 (458.75 eV) and Pt–TiO_2 (458.78 eV), indicating electron transfer between the NPs and TiO_2. In contrast, Au–TiO_2 (458.69 eV) and Ag–TiO_2 (458.67 eV) exhibit a more pronounced Ti^{3+} signal at ∼457.5 eV, suggesting an increase in oxygen vacancies and partial reduction of Ti^{4+}. This electronic modification is known to enhance charge carrier mobility. The variations in satellite peak intensity further support these electronic changes [60].

Moreover, subtle shifts in the primary O1s peak (Fig. S6 (O1s)) corresponding to lattice oxygen (O–Ti–O) are observed in the spectra of all metal-loaded samples. In Pt–TiO_2 (530.76 eV) and Pd–TiO_2 (530.75 eV), the binding energy is slightly higher compared to bare TiO_2

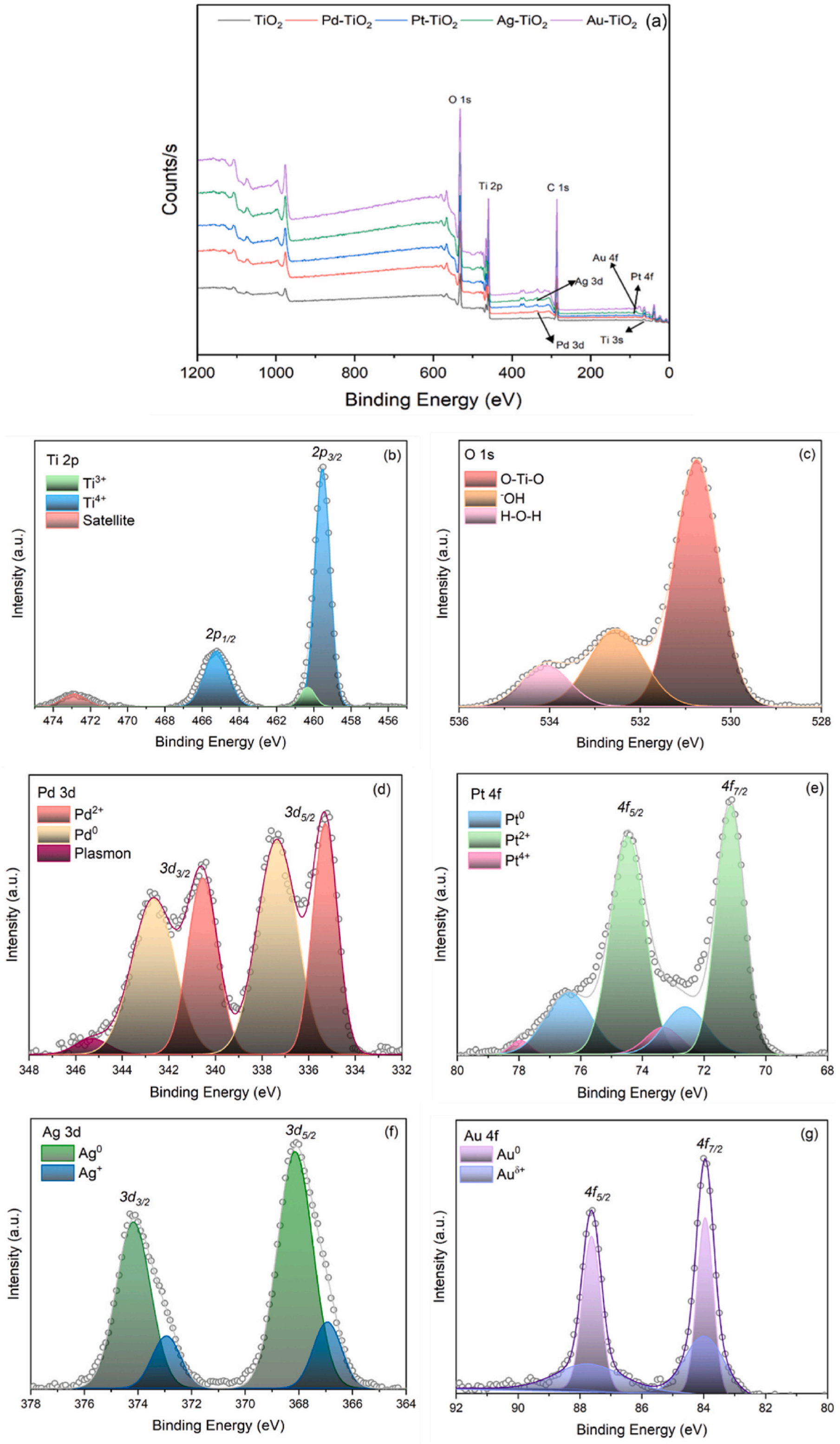

Fig. 2. XPS analysis of metal-loaded TiO_2. **(a)** XPS survey, **(b)** Ti 2p, **(c)** O 1s, **(d)** Pd 3d, **(e)** Pt 4f, **(f)** Au, 4f, **(g)** Ag 3d.

(530.63 eV), indicating electron withdrawal by these metals. This electron depletion reduces the electron density around oxygen, thereby stabilizing the Ti–O bond. In contrast, Au–TiO_2 (530.45 eV) and Ag–TiO_2 (530.63 eV) exhibit a lower or comparable binding energy, suggesting electron donation from these metals, leading to a slightly more reduced state [61].

The peaks at ~532–535 eV, corresponding to hydroxyl groups (-OH) and molecularly adsorbed water (H_2O), also show intensity and position variations. Pt–TiO_2 (532.77 eV) and Pd–TiO_2 (532.55 eV) exhibit stronger hydroxyl signals, indicating enhanced surface hydroxylation, likely due to increased water dissociation facilitated by these metals. On the other hand, Au–TiO_2 (532.88 eV) and Ag–TiO_2 (532.20 eV) display lower hydroxyl intensities, implying reduced surface hydroxylation [62].

The TEM and HRTEM images presented in Fig. 3 provide insights into the morphology, dispersion, and crystalline structures of the metal-decorated TiO_2 nanocomposites, while the corresponding particle size distributions offer quantitative analysis of the nanoparticle sizes.

TEM images (Fig. 3a–d, g, j) confirm the successful deposition of metal nanoparticles on TiO_2. Ag–TiO_2 and Au–TiO_2 display larger, well-dispersed nanoparticles, with Ag exhibiting a more irregular morphology. In contrast, Pd–TiO_2 and Pt–TiO_2 show smaller, more uniformly distributed particles, indicating enhanced dispersion.

HRTEM images (Fig. 3b–e, h, k) reveal clear lattice fringes in all samples, confirming high crystallinity. Distinct fringes corresponding to both the metal and TiO_2 phases further validate the successful nanoparticle incorporation. Particle size distributions (Fig. 3c–f, i, l) indicate that Ag–TiO_2 and Au–TiO_2 exhibit broader size ranges (20–110 nm and 10–90 nm, respectively), while Pd–TiO_2 and Pt–TiO_2 feature smaller, more uniform particles (~14 nm and ~5 nm, respectively). These results

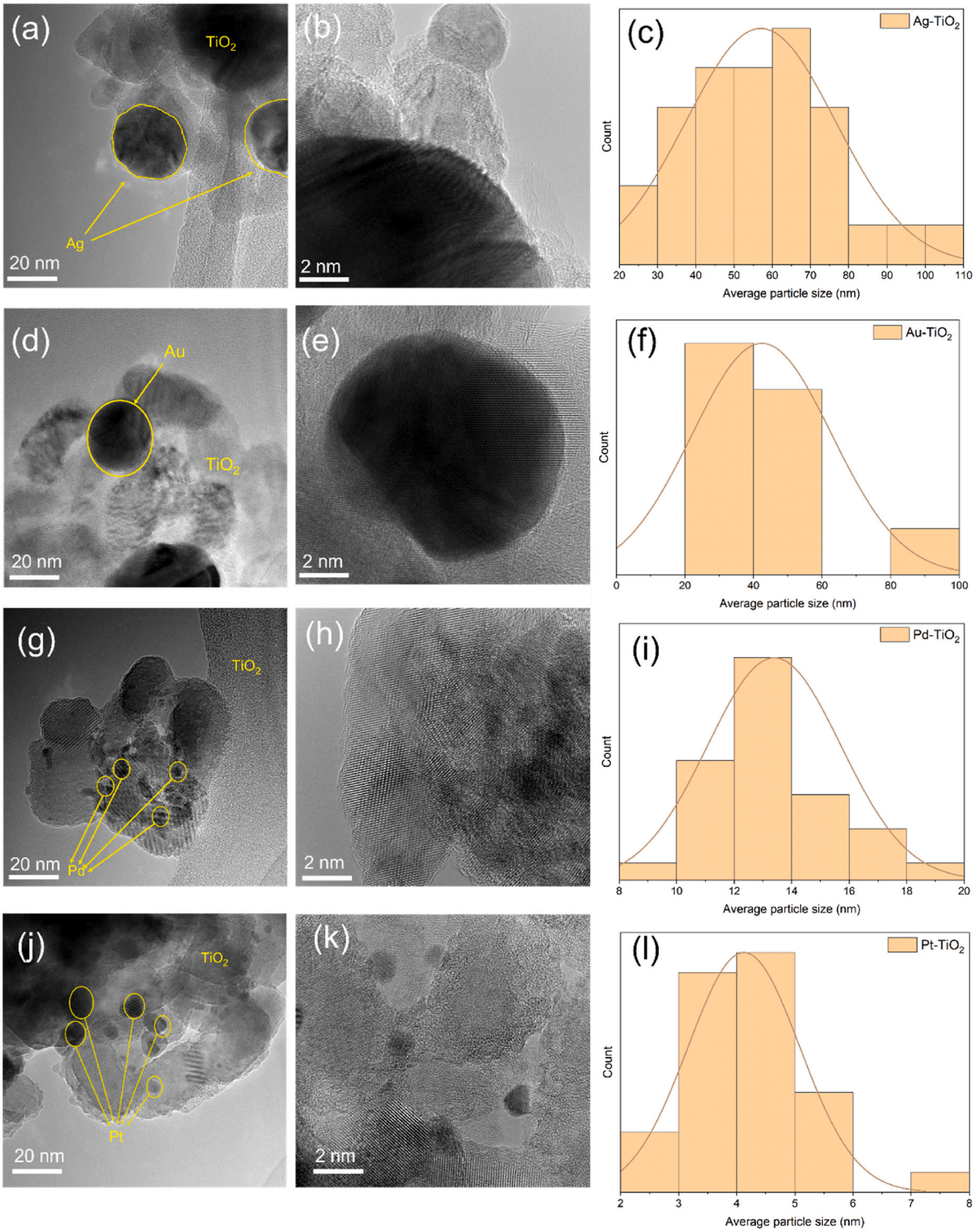

Fig. 3. Typical TEM and HRTEM images of Ag–TiO_2 (a, b), Au–TiO_2 (d, e), Pd–TiO_2 (g, h), and Pt–TiO_2 (j, k); particle size distributions of Ag–TiO_2 (c), Au–TiO_2 (f), Pd–TiO_2 (i), and Pt–TiO_2 (l).

align with the XRD analysis, which also indicates that Pt forms the smallest particles, followed by Pd, Au, and Ag.

The elemental distribution in TiO_2 samples doped with noble metals was evaluated using STEM/EDS mapping mode (Fig. 4). Pd and Pt appear to be evenly dispersed on the TiO_2 surface, while the Ag and Au nanoparticles distribution is less well distributed. The EDX analysis of Ag and Au samples were moreover confirmed. The Cu peaks observed in the EDX spectra are attributed to the use of copper tape for sample preparation. Furthermore, small amounts of gold and silver were detected in their volumes. The standard deviation for gold and silver samples were very high (i.e., 19.56 and 20.37) against 2.31 and 0.96 for Pd and Pt nanoparticles, respectively. This indicates the agglomeration and non-uniform distribution of Ag and Au nanoparticles in the catalysts volume. This result is in agreement with the HR-TEM analysis, which shows few but large Au and Ag particles, compared to small and evenly distributed Pt and Pd particles.

We used DFT calculations to evaluate the stability of several model metal clusters adsorbed on the TiO_2 surface. The adsorption and cohesive energies calculated for the four investigated TM clusters is reported in Fig. 5. In all cases both the calculated adsorption and cohesive

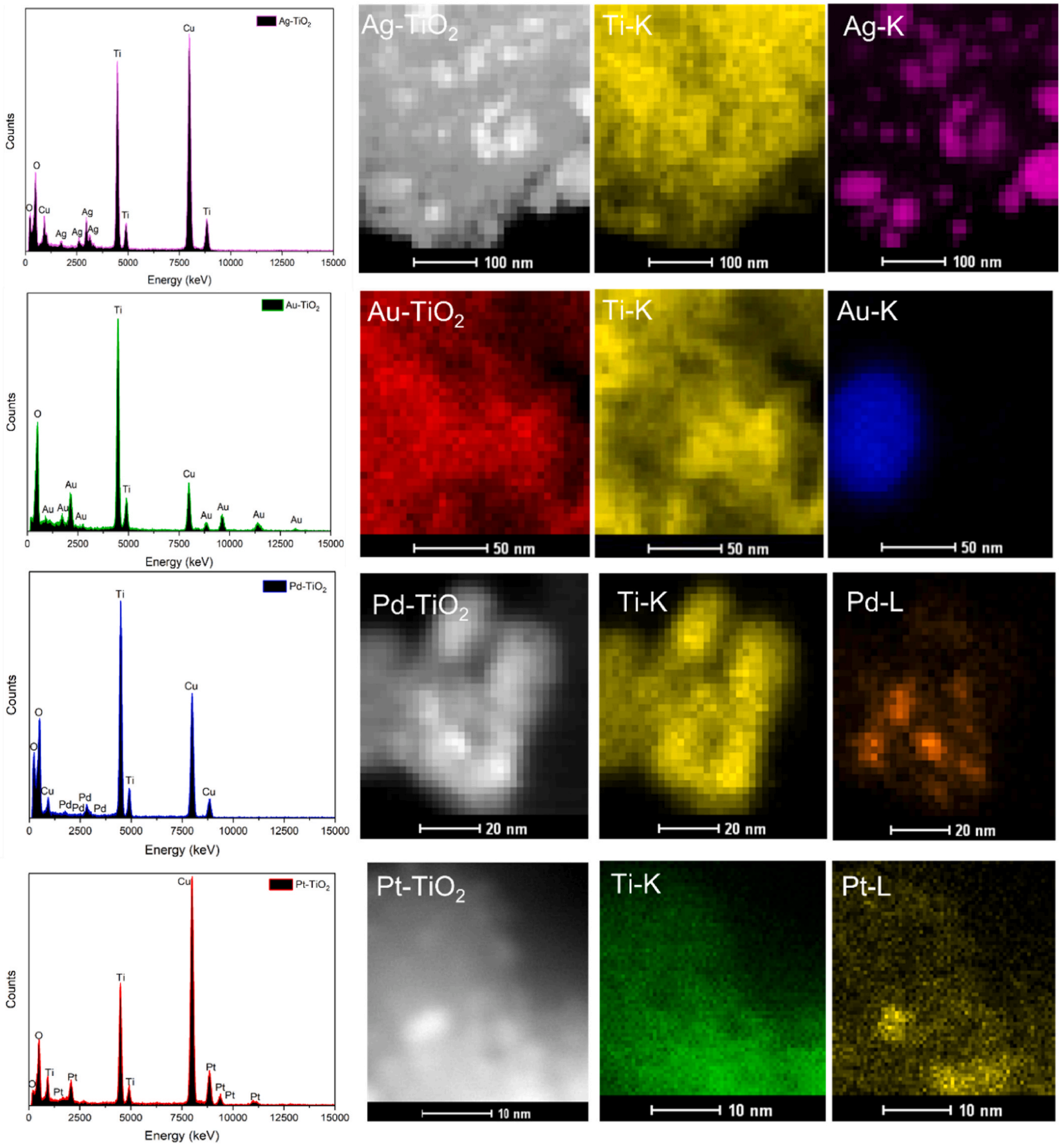

Fig. 4. HDAAF-STEM EDX of (**a**) Ag–TiO_2, (**b**) Au–TiO_2, (**c**) Pd–TiO_2, (**d**) Pt–TiO_2.

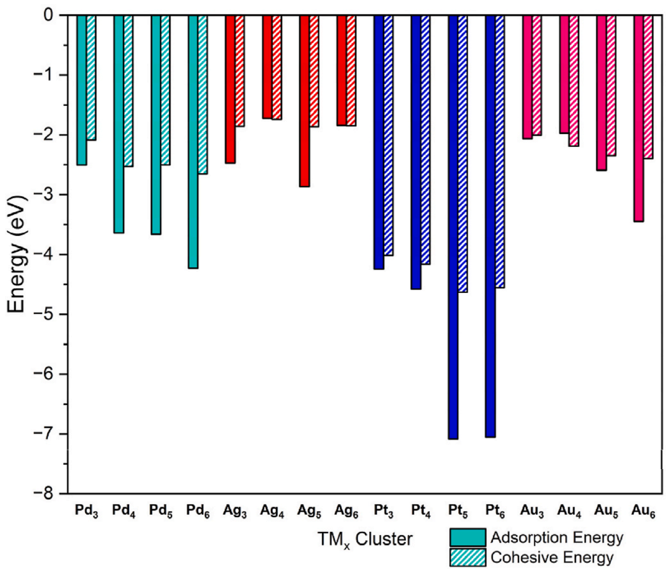

Fig. 5. Adsorption (solid bars) and cohesive (dashed bars) energies of different metal clusters (TM_x) on anatase (101) surface.

energies are negative, indicating the stability of the metal clusters on the host substrate [63]. The metal adsorption energies for the trimer clusters range from −2.0 eV to −4.2 eV, with Pt exhibiting the most favourable adsorption value. These values are within the range of other calculated adsorption energies reported in the literature [64–66]. It is worth noting that in the case of Pt and Pd clusters the adsorption energies are consistently and significantly more negative than the corresponding cohesive energies. This indicates a preference for these metals to form smaller and more dispersed nanoparticles. In contrast, Au and Ag exhibit adsorption and cohesive energies of similar magnitude, suggesting a more pronounced tendency for these metals to agglomerate. These trends align well with the experimentally observed nanoparticle sizes shown in Fig. 3.

In order to determine the specific surface area and assess the porosity of the photocatalysts, BET N_2 adsorption/desorption measurements were carried out (Fig. S8, Table S4). Based on the IUPAC classification, the isotherms of the synthesized catalysts can be classified as type IV isotherms [67]. This characteristic is typical of mesoporous adsorbents and indicates monolayer adsorption at low pressures and multilayer adsorption at higher pressures. The separation of the adsorption-desorption branches at low pressure ($P/P_0 = 0.1$) suggests that capillary condensation, represented by type H3 hysteresis loops, begins at lower pressures in these samples. The metal photodeposition reduces the specific surface area and the total pore volume compared to pristine TiO_2. This can be associated to alterations in the morphology, crystalline structure, and size [68,69]. The addition of Ag resulted in a strong decrease in the peak from 146 Å for bare TiO_2 to 86 Å. This decrease can be attributed to metal particles blocking the pores, thereby reducing the overall surface area available for nitrogen adsorption in the BET experiment. In contrast, the addition of Pd slightly increased the peak to 153 Å. This increase is likely due to the highly dispersed Pd nanoparticles on the TiO_2 surface, which not only preserve the pore structure but may also create new nanopores with a radius of approximately 15.3 nm, thus decreasing the overall surface area.

The optical characteristics of TiO_2 particles, both pure and those loaded with noble metals, were examined using UV–vis DRS, as depicted Fig. 6a. The DRS spectra span from 200 to 800 nm. Unlike bare TiO_2, the noble metal-loaded TiO_2 particles exhibit visible light absorption. This broad absorption feature is due to the surface plasmon resonance of the noble metal nanoparticles. The introduction of Pd, Pt, Au, and Ag into TiO_2 lattice increases the likelihood of electron transitions from the valence band to the conduction band [70]. Moreover, the localized surface plasmonic resonance (LSPR) effect of Ag, Au, Pt, and Pd nanoparticles further improves the solar energy conversion efficiency. This enhancement is achieved by broadening light absorption to longer wavelengths, light scattering increase, and promotion of the photogenerated carriers in the semiconductor through the transfer of plasmonic energy from the noble metal nanoparticle to the semiconductor. However, it is worth noting that, in some cases, surface-located metal nanoparticles may serve as recombination sites [71].

According to Sellappan et al. [72], and Ghosh et al. [73], the LSPR effect in Ag–TiO_2 and Au–TiO_2 photocatalysts is influenced by the number of nanoparticles on the TiO_2 surface. Increasing Ag and Au ion concentrations during the catalyst preparation results in a red shift in the LSPR band of their absorption spectra. Besides, the photoconversion quantum yield may be improved by modification of the photocatalyst using noble metal nanoparticles (e.g., Pt) [74]. This finding might be explained considering two distinct phenomena: (i) the existence of Ti^{3+}, as a result of platinum being deposited on the TiO_2 surface; and (ii) the establishment of the Schottky barrier at the interface between Pt and TiO_2, which prevents the recombination of the photogenerated charge carriers [70].

To better understand the behavior of the electron-hole pairs in the semiconductor particles, the effectiveness of charge migration and carrier trapping has been investigated using PL spectroscopic technology. Fig. 6b shows the PL spectra of bare TiO_2 and representative metal-

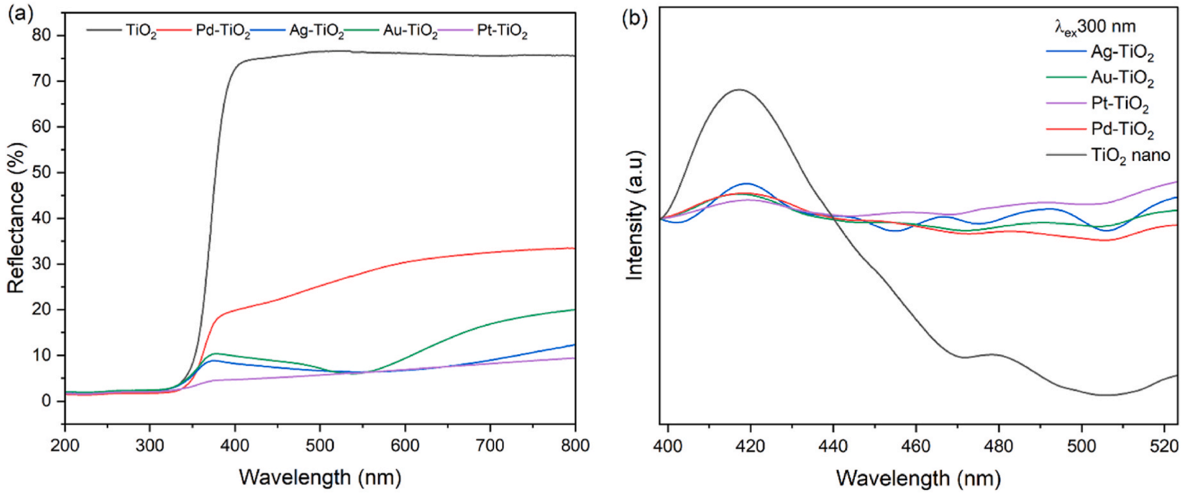

Fig. 6. **(a)** UV–vis diffuse reflectance spectra of bare and metal-loaded TiO_2, **(b)** Photoluminescence spectra of bare and metal-loaded TiO_2.

loaded TiO_2, after background subtraction.

The primary emission peak observed around 420–423 nm can be ascribed to the band-to-band transition taking place owing to the migration of electrons from the semiconductor's conduction band back to the valence band [43]. A distinguished reduction in the main emission peak is noted with the doping of Ag, Pd, Pt and Au into TiO_2 surface. Thus, although noble metals do not induce new PL phenomena, they reduce the excitonic PL intensity. This was attributed to the capture of photoexcited electrons or holes by the metal ions. Consequently, in noble metal-loaded systems, the lower excitonic PL intensity is indicative of a higher rate of photo-induced charge carrier separation [75,76]. It can be seen in Fig. 6b that the extent of PL quenching varies depending on the metal type. Specifically, the addition of Pt, Au, and Pd results in a significant reduction in PL intensity compared to Ag deposition and bare TiO_2, while the addition of Ag results in a moderate reduction in PL intensity. Therefore, surface modification with Au, Pt, Pd and Ag can effectively suppress the recombination process of the photogenerated carriers in TiO_2, in the following order of effectiveness: Pt > Pd ≈ Au > Ag > bare TiO_2.

To further validate the impact of noble metal incorporation on the charge transfer dynamics, an electrochemical impedance spectroscopy (EIS) test was conducted as depicted in Fig. S7 and Table S3. Pristine TiO_2 exhibits the highest R_{ct} value of 152 kΩ, confirming its poor electrical conductivity and inefficient charge transfer. Doping with noble metals significantly reduces R_{ct}, with Ag–TiO_2 (0.15 kΩ) and Pd–TiO_2 (0.71 kΩ) showing the most pronounced improvements, suggesting enhanced charge transport facilitated by the formation of Schottky junctions [77]. Pt–TiO_2 also demonstrates a substantially lower R_{ct} (7.52 kΩ) compared to bare TiO_2, whereas Au–TiO_2 exhibits a moderate reduction to 87.7 kΩ, indicating relatively limited conductivity enhancement [78]. The trends in the constant phase element (CPE) values, presented in Table S3, further support these findings. Pristine TiO_2 exhibits the highest capacitance (50.7 μF), indicative of greater charge accumulation and recombination, while noble metal-doped samples such as Pt–TiO_2 (0.131 μF) and Pd–TiO_2 (0.163 μF) display significantly lower CPE values, reflecting improved charge separation [79].

3.2. Photocatalyst activity

Fig. 7a shows the photocatalytic hydrogen production rate in the presence of different metals (i.e., Ag, Pd, Au, Pt) photodeposited on TiO_2, using methanol as the sacrificial agent, under UV and visible light irradiation. As clearly indicated in the figure, the loading of Pt resulted in the best performance in terms of hydrogen evolution, reaching a hydrogen production rate of 28 mmol/h g, which is about 35-fold higher than bare TiO_2. In contrast, Ag shows the lowest hydrogen productivity compared to the other metals, resulting in a hydrogen production rate of approximately 2 mmol/h g. Overall, the H_2 evolution under UV/visible irradiation follows the trend: Pt > Au ≈ Pd > Ag > bare TiO_2.

The particle size of metal nanoparticles plays a critical role in the photocatalytic hydrogen production efficiency of metal-decorated TiO_2 nanocomposites [80]. Smaller nanoparticles typically exhibit a higher surface area-to-volume ratio, which increases the number of active sites available for the hydrogen evolution reaction (HER) and enhances charge separation by acting as electron sinks [81]. This often leads to improved hydrogen production rates, with small nanoparticles demonstrating superior catalytic activity due to their high work function and near-zero overpotential for HER [82]. The enhanced performance of Pt and the relatively weaker performance of Ag under UV/visible light observed in Fig. 7a align with the observed nanoparticle sizes (see Fig. 3). However, the performance trend cannot be solely attributed to nanoparticle sizes, indicating that other factors should be taken into account. The H_2 evolution trend under UV/visible light is consistent with the suppression of the photogenerated charge recombination, as evidenced by the PL measurements in Fig. 6b. A slightly different trend was observed under visible light irradiation (Fig. 7b), with Pd exhibiting the highest activity amongst the investigated metals. This sample is the one exhibiting the least extent of PL low energy emission (430–500 nm), likely correlated to a lower density of intraband gap states working as detrimental recombination sites [83]. The lower density of these gap states implies that under visible light, the concentration of catalytically active photoholes is rate limiting, with Pd displaying the longest lifetimes out of all metals, which promotes steps 2–3, 4–5, and 7–8 in Fig. S9, resulting in higher hydrogen production. All the metal-loaded samples demonstrated a measurable H_2 production rate under visible light irradiation, although this was substantially lower than under UV/visible light, where hydrogen radical coupling is the rate limiting factor.

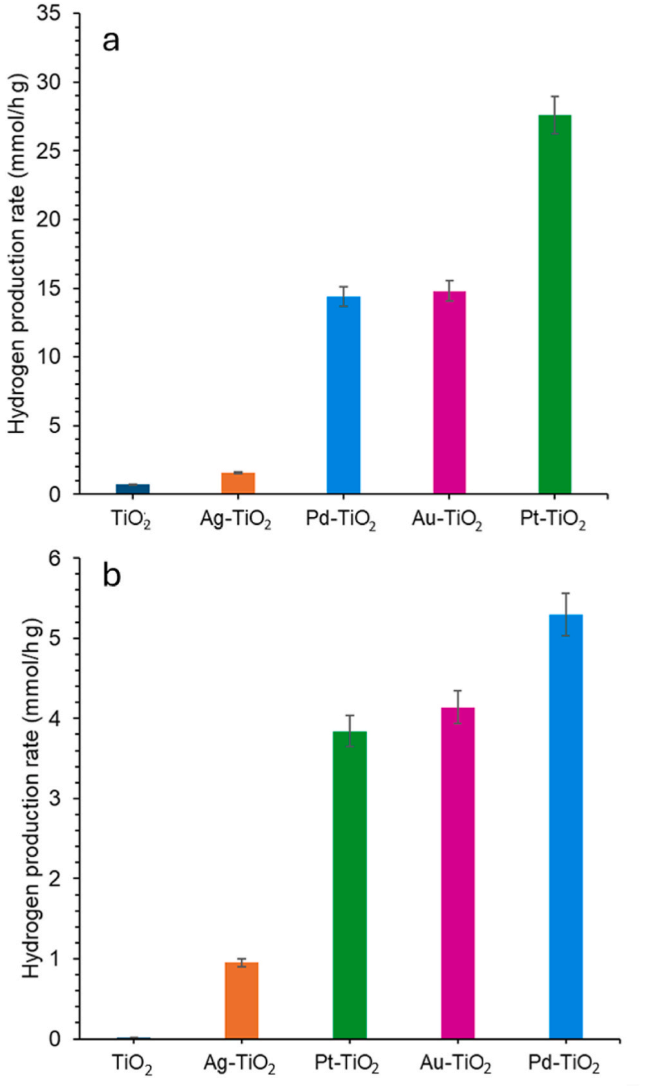

Fig. 7. Hydrogen production rate in the presence of bare and metal-loaded photocatalysts under **(a)** UV/visible and **(b)** visible light irradiation. Experimental conditions: [Catalyst] = 500 ppm; [Methanol] = 2.5 M; neutral pH; T = 25 °C.

Reactant species, such as methanol or water, may initially undergo thermal dissociation, generating surface anions and protons. Under suitable photocatalytic conditions, methoxy and hydroxyl anions can capture holes, while protons migrate to co-catalysts to capture electrons, leading to the formation of surface radicals. Hydrogen radicals can subsequently combine to form molecular hydrogen, which desorbs from the surface, while methoxy and hydroxyl radicals undergo further oxidation, producing additional protons during steps 3–4 and 6–7

(Fig. S9). The reaction mechanism remains consistent under both UV/visible and visible light irradiation; however, the lower activity observed under visible light is attributed to the reduced concentration and shorter lifetimes of charge carriers, reducing the likelihood of steps 2–3, 4–5, and 7–8 occurring.

To elucidate the mechanism of charge transfer upon hydrogen adsorption on the TM, we evaluated the change in electron density upon adsorption of hydrogen on a model TM_3/TiO_2 system. Fig. 8 shows the charge density distribution plots (CDDs) for the investigated TMs. When hydrogen adsorbs on Pt, Au, and Pd, migration of electrons from the adsorbed hydrogen to the TM cluster is observed. In these cases, electron depletion regions appear on top of the adsorbed hydrogen atom. In contrast, when hydrogen adsorbs on Ag, there is significant electron transfer from TiO_2 and the TM cluster to the adsorbed hydrogen. Fig. 9 shows the Gibbs free energies of hydrogen adsorption on the TM_3/TiO_2 clusters (ΔG_H) calculated using Equation (4). Qualitative correlations can be observed between charge transfer and hydrogen adsorption Gibbs free energies: Pt, Au, and Pd, which gain some electron density from hydrogen, have zero or small negative hydrogen adsorption energies, while Ag, which lose electron density to hydrogen, have large positive ΔG_H values. According to the Sabatier principle, a photocatalyst active site with a ΔG_H close to zero presents the most promising activity towards the hydrogen evolution reaction rate [84]. In this context, a single hydrogen atom must not adsorb too weakly ($\Delta G_H \gg 0$) nor too strongly ($\Delta G_H \ll 0$) to avoid a significant energy barrier to reaction.

As observed in Fig. 9, Pt exhibits an absolute ΔG_H value close to 0. Consistent with the Sabatier principle, Pt provides the highest hydrogen production rate amongst the investigated metals. Both Au and Pd show similar small negative ΔG_H values. These metals also achieve relatively high hydrogen production rates. In contrast, a large positive value of ΔG_H for Ag (0.92 eV) aligns with the lowest hydrogen production rate observed experimentally. By comparing Fig. 7a and b, we observe that hydrogen radical coupling on Ag remains the rate limiting step, discounting any benefit in additional absorbance of visible light when compared to other metals. This analysis suggests that ΔG_H is a critical descriptor for evaluating the activity of a photocatalytic material in hydrogen production.

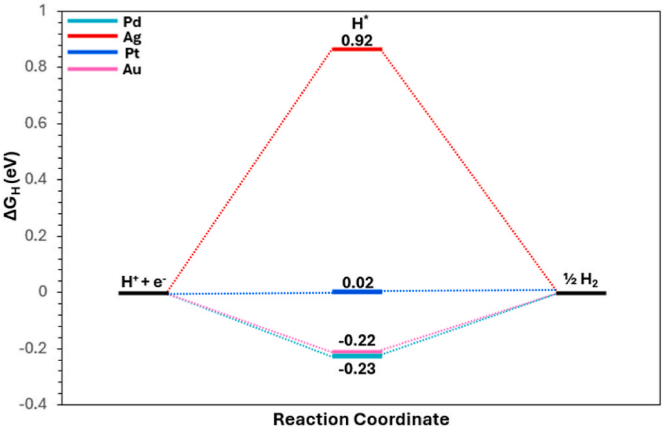

Fig. 9. Reaction coordinate diagram showing the Gibbs free energy for hydrogen evolution reaction on different model TM_3/TiO_2 systems. H* stands for hydrogen adsorbed on TM_3/TiO_2.

4. Conclusion

This study provides a comprehensive analysis of the photocatalytic performance of anatase TiO_2 loaded with various noble metals, such as Pt, Au, Pd, and Ag. Through a combination of experimental and computational approaches, we have elucidated the main factors through

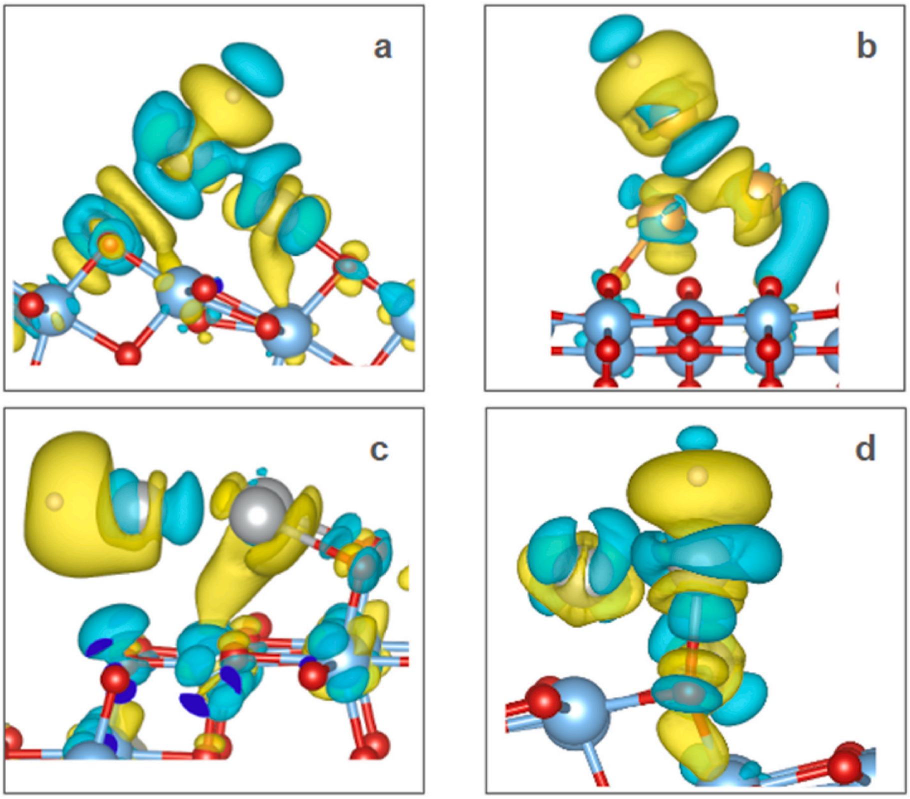

Fig. 8. Charge density distribution plots for hydrogen adsorbed on Pt **(a)**, Au **(b)**, Ag **(c)**, and Pd **(d)** model TM_3/TiO_2 structures. The yellow region represents electron accumulation, and the blue region represents electron depletion. (Isosurface value = 0.0011 $bohr^{-3}$). (For interpretation of the references to colour in this figure legend, the reader is referred to the Web version of this article.)

which these co-catalysts influence the charge carrier dynamics, light absorption properties, and overall hydrogen production efficiencies of TiO_2 photocatalyst. The hydrogen production rate under simultaneous UV and visible light irradiation followed the trend Pt $>$ Au $\approx$ Pd $>$ Ag $>$ bare TiO_2. Among the co-catalysts, Pt and Pd were well distributed on the TiO_2 surface and formed the smallest nanoparticles, while Ag and Au exhibited less uniform distribution. All noble metal-loaded TiO_2 samples showed enhanced absorption in the visible region, primarily due to the surface plasmon resonance of the metal nanoparticles. Pt, Au, and Pd were particularly effective in suppressing the electron-hole recombination process, as evidenced by the significant reduction in photoluminescence intensity compared to Ag deposition and bare TiO_2. The effectiveness in suppressing the electron-hole recombination followed the order Pt $>$ Pd $\approx$ Au $>$ Ag $>$ bare TiO_2.

Additionally, our DFT calculations showed that hydrogen adsorption on Pt, Au, and Pd co-catalyst clusters results in the electron transfer from the adsorbed hydrogen to the metal cluster. The analysis of Gibbs free energies of hydrogen adsorption revealed a correlation between adsorption Gibbs energies and hydrogen production rates, confirming the order of effectiveness as Pt $>$ Pd $\approx$ Au $>$ Ag. In conclusion, this study underscores the critical role of metal co-catalysts in optimizing the photocatalytic performance of TiO_2 for hydrogen production, with Pt emerging as the most effective due to its superior charge carrier management, stability, and interaction with hydrogen. This research provides a framework based on the combination of experimental and computational methods for the design and development of novel photocatalysts based on the combination of semiconductors with transition metals for sustainable applications.

CRediT authorship contribution statement

Sarah Hamdan: Writing – original draft, Investigation, Data curation. **Matthew J. Wigglesworth:** Writing – original draft, Investigation, Formal analysis. **Marica Muscetta:** Writing – review & editing, Methodology, Data curation, Conceptualization. **Ruiman Ma:** Writing – original draft, Investigation, Data curation. **Mohamed I. Helal:** Investigation, Data curation. **Natalia Martsinovich:** Writing – review & editing, Supervision, Project administration, Conceptualization. **Giovanni Palmisano:** Writing – review & editing, Supervision, Project administration, Conceptualization. **Sergio Vernuccio:** Writing – review & editing, Supervision, Funding acquisition, Conceptualization.

Declaration of competing interest

The authors declare that they have no known competing financial interests or personal relationships that could have appeared to influence the work reported in this paper.

Acknowledgments

This paper is based upon work supported primarily by the Royal Society International Exchange grant (IES\R3\203083) and by the Worldwide University Network (WUN) Research Development Fund. Khalifa University funding is also acknowledged through the Research and Innovation Centre on CO_2 and Hydrogen (RICH centre), project RC2-2019-007. Dr. Thomas Delclos (Khalifa University) is acknowledged for support in XPS characterizations.

Appendix A. Supplementary data

Supplementary data to this article can be found online at https://doi.org/10.1016/j.ijhydene.2025.03.184.

References

[1] Fang S, Liu Y, Sun Z, Lang J, Bao C, Hu YH. Photocatalytic hydrogen production over Rh-loaded TiO2: what is the origin of hydrogen and how to achieve hydrogen production from water? Appl Catal, B Dec. 2020;278. https://doi.org/10.1016/j.apcatb.2020.119316.

[2] Corredor J, Rivero MJ, Rangel CM, Gloaguen F, Ortiz I. Comprehensive review and future perspectives on the photocatalytic hydrogen production. John Wiley and Sons Ltd; Oct. 01, 2019. https://doi.org/10.1002/jctb.6123.

[3] Christoforidis KC, Fornasiero P. Photocatalytic hydrogen production: a rift into the future energy supply. ChemCatChem 2017;9(9):1523–44. https://doi.org/10.1002/cctc.201601659.

[4] Chi J, Yu H. Water electrolysis based on renewable energy for hydrogen production. Cuihua Xuebao/Chinese Journal of Catalysis 2018;39(3):390–4. https://doi.org/10.1016/S1872-2067(17)62949-8.

[5] Kovač A, Marciuš D, Budin L. Solar hydrogen production via alkaline water electrolysis. Int J Hydrogen Energy 2019;44(20):9841–8. https://doi.org/10.1016/j.ijhydene.2018.11.007.

[6] Banerjee D, Kushwaha N, Shetti NP, Aminabhavi TM, Ahmad E. Green hydrogen production via photo-reforming of bio-renewable resources. Elsevier Ltd.; Oct. 01, 2022. https://doi.org/10.1016/j.rser.2022.112827.

[7] Bumajdad A, Madkour M. Understanding the superior photocatalytic activity of noble metals modified titania under UV and visible light irradiation. Royal Society of Chemistry; Apr. 28, 2014. https://doi.org/10.1039/c3cp54411g.

[8] Muscetta M, Andreozzi R, Clarizia L, Di Somma I, Marotta R. Hydrogen production through photoreforming processes over Cu2O/TiO2 composite materials: a mini-review. Elsevier Ltd.; Oct. 30, 2020. https://doi.org/10.1016/j.ijhydene.2020.07.225.

[9] Muscetta M, et al. Visible light – driven photocatalytic hydrogen production using Cu2O/TiO2 composites prepared by facile mechanochemical synthesis. J Environ Chem Eng Jun. 2022;10(3):107735. https://doi.org/10.1016/j.jece.2022.107735.

[10] Yang Z, Huang T, Li M, Wang X, Zhou X, Yang S, Gao Q, Cai X, Liu Y, Fang Y, Wang Y, Zhang S, Zhang S. Unveiling the synergistic role of frustrated Lewis pairs in carbon-encapsulated Ni/NiOx photothermal cocatalyst for enhanced photocatalytic hydrogen production. Adv Mat 2024;36:2313513. https://doi.org/10.1002/adma.202313513.

[11] Yang Z, Li M, Chen S, Yang S, Peng F, Liao J, Fang Y, Zhang S, Zhang S. "Cocatalyst engineering with robust tunable carbon-encapsulated Mo-rich Mo/Mo2C heterostructure nanoparticle for efficient photocatalytic hydrogen. Evolution 2023;33:2212746. https://doi.org/10.1002/adfm.202212746.

[12] Ibrahim NS, Leaw WL, Mohamad D, Alias SH, Nur H. A critical review of metal-doped TiO2 and its structure–physical properties–photocatalytic activity relationship in hydrogen production. Elsevier Ltd.; Oct. 30, 2020. https://doi.org/10.1016/j.ijhydene.2020.07.233.

[13] Jiménez-Calvo P, Caps V, Keller V. Plasmonic Au-based junctions onto TiO2, gC3N4, and TiO2-gC3N4 systems for photocatalytic hydrogen production: fundamentals and challenges. Elsevier Ltd.; Oct. 01, 2021. https://doi.org/10.1016/j.rser.2021.111095.

[14] Muscetta M, et al. Hydrogen production upon UV-light irradiation of Cu/TiO 2 photocatalyst in the presence of alkanol- amines. Int J Hydrogen Energy 2020;45 (51). https://doi.org/10.1016/j.ijhydene.2020.07.002.

[15] Reddy NL, et al. A review on frontiers in plasmonic nano-photocatalysts for hydrogen production. Int J Hydrogen Energy Apr. 2019;44(21):10453–72. https://doi.org/10.1016/j.ijhydene.2019.02.120.

[16] Ran J, Zhang J, Yu J, Jaroniec M, Qiao SZ. Earth-abundant cocatalysts for semiconductor-based photocatalytic water splitting. Royal Society of Chemistry; Nov. 21, 2014. https://doi.org/10.1039/c3cs60425j.

[17] Kumaravel V, Mathew S, Bartlett J, Pillai SC. Photocatalytic hydrogen production using metal doped TiO2: a review of recent advances. Elsevier B.V.; May 05, 2019. https://doi.org/10.1016/j.apcatb.2018.11.080.

[18] Bai S, Zhang N, Gao C, Xiong Y. Defect engineering in photocatalytic materials. Elsevier Ltd.; Nov. 01, 2018. https://doi.org/10.1016/j.nanoen.2018.08.058.

[19] Beasley C, et al. Effect of metal work function on hydrogen production from photocatalytic water splitting with MTiO2 catalysts. ChemistrySelect Jan. 2020;5 (3):1013–9. https://doi.org/10.1002/SLCT.201904151.

[20] Vega L, Bahamon D, Sinnokrot M, Li Y, Vega LF. "Computational screening of transition metal-doped CdS for photocatalytic hydrogen production. Computational screening of transition metal-doped CdS for photocatalytic hydrogen production,". 2022. https://doi.org/10.21203/rs.3.rs-1796805/v1.

[21] Assadi MHN, Hanaor DAH. The effects of copper doping on photocatalytic activity at (101) planes of anatase TiO 2 : a theoretical study. Appl Surf Sci Nov. 2016;387: 682–9. https://doi.org/10.1016/j.apsusc.2016.06.178.

[22] Wen L, Liu B, Zhao X, Nakata K, Murakami T, Fujishima A. Synthesis, characterization, and photocatalysis of Fe-doped TiO 2: a combined experimental and theoretical study. Int J Photoenergy 2012;2012. https://doi.org/10.1155/2012/368750.

[23] Nolan M, Iwaszuk A, Lucid AK, Carey JJ, Fronzi M. Design of novel visible light active photocatalyst materials: surface modified TiO2. Adv Mater Jul. 2016;28(27): 5425–46. https://doi.org/10.1002/adma.201504894.

[24] Suman, et al. Understanding the role of Ni ions on the photocatalytic activity and dielectric properties of hematite nanostructures: an experimental and DFT approach. J Phys Chem Solid 2021;156(Sep). https://doi.org/10.1016/j.jpcs.2021.110118.

[25] Belhacova L, Bibova H, Marikova T, Kuchar M, Zouzelka R, Rathousky J. Removal of ampicillin by heterogeneous photocatalysis: combined experimental and dft study. Nanomaterials Aug. 2021;11(8). https://doi.org/10.3390/nano11081992.

[26] Basavarajappa PS, Patil SB, Ganganagappa N, Reddy KR, Raghu AV, Reddy CV. Recent progress in metal-doped TiO2, non-metal doped/codoped TiO2 and TiO2 nanostructured hybrids for enhanced photocatalysis. Int J Hydrogen Energy 2020; 45(13):7764–78. https://doi.org/10.1016/j.ijhydene.2019.07.241.

[27] Ma R, Williams G, Muscetta M, Vernuccio S. Enhanced photocatalytic hydrogen evolution via ball-milled PtO2/TiO2 heterojunction photocatalyst: an alternative approach for efficient energy production. Chem Eng J Mar. 2025;507:160228. https://doi.org/10.1016/j.cej.2025.160228.

[28] Qu S, Ma R, Efimov I, Hadjittofis E, Vernuccio S, Sedransk Campbell K. Understanding and tuning Fe-doping on Zn–Fe layered double hydroxide particle and photocatalytic properties. Adv Energ Sust Res 2025:2400309. https://doi.org/10.1002/aesr.202400309.

[29] Kresse G, Furthmüller J. Efficient iterative schemes for ab initio total-energy calculations using a plane-wave basis set. Phys Rev B Oct. 1996;54(16):11169. https://doi.org/10.1103/PhysRevB.54.11169.

[30] Kresse G, Furthmüller J. Efficiency of ab-initio total energy calculations for metals and semiconductors using a plane-wave basis set. Comput Mater Sci Jul. 1996;6(1): 15–50. https://doi.org/10.1016/0927-0256(96)00008-0.

[31] Perdew JP, Burke K, Ernzerhof M. Generalized gradient approximation made simple. Phys Rev Lett Oct. 1996;77(18):3865. https://doi.org/10.1103/PhysRevLett.77.3865.

[32] Blöchl PE. Projector augmented-wave method. Phys Rev B Dec. 1994;50(24): 17953. https://doi.org/10.1103/PhysRevB.50.17953.

[33] Kresse G, Joubert D. From ultrasoft pseudopotentials to the projector augmented-wave method. Phys Rev B Jan. 1999;59(3):1758. https://doi.org/10.1103/PhysRevB.59.1758.

[34] Grimme S, Ehrlich S, Goerigk L. Effect of the damping function in dispersion corrected density functional theory. J Comput Chem May 2011;32(7):1456–65. https://doi.org/10.1002/JCC.21759.

[35] Grimme S, Antony J, Ehrlich S, Krieg H. A consistent and accurate ab initio parametrization of density functional dispersion correction (DFT-D) for the 94 elements H-Pu. J Chem Phys Apr. 2010;132(15). https://doi.org/10.1063/1.3382344/926936.

[36] Dudarev SL, Botton GA, Savrasov SY, Humphreys CJ, Sutton AP. Electron-energy-loss spectra and the structural stability of nickel oxide: an LSDA+U study. Phys Rev B Jan. 1998;57(3):1505. https://doi.org/10.1103/PhysRevB.57.1505.

[37] Hu Z, Metiu H. Choice of U for DFT+ U calculations for titanium oxides. J Phys Chem C Apr. 2011;115(13):5841–5. https://doi.org/10.1021/JP111350U/ASSET/IMAGES/MEDIUM/JP-2010-11350U_0003.GIF.

[38] Wang V, Xu N, Liu JC, Tang G, Geng WT. VASPKIT: a user-friendly interface facilitating high-throughput computing and analysis using VASP code. Comput Phys Commun Oct. 2021;267:108033. https://doi.org/10.1016/J.CPC.2021.108033.

[39] Jinli Z, Ming Z, You H, Wei L, Xiangkun M, Baoning Z. Nucleation and Growth of palladium clusters on anatase TiO2(101) surface: a first principle study. J Phys Chem C Dec. 2008;112(49):19506–15. https://doi.org/10.1021/JP8036523/SUPPL_FILE/JP8036523_SI_001.PDF.

[40] Han Y, Liu CJ, Ge Q. Interaction of Pt clusters with the anatase TiO2(101) surface: a first principles study. J Phys Chem B Apr. 2006;110(14):7463–72. https://doi.org/10.1021/JP0608574.

[41] Gong XQ, Selloni A, Dulub O, Jacobson P, Diebold U. Small Au and Pt clusters at the anatase TiO2(101) surface: behavior at terraces, steps, and surface oxygen vacancies. J Am Chem Soc Jan. 2008;130(1):370–81. https://doi.org/10.1021/ja0773148.

[42] Ishikawa R, Futazuka T, Jimbo Y, Kawahara K, Shibata N, Ikuhara Y. Real-time tracking of three-dimensional atomic dynamics of Pt trimer on TiO2 (110). Sci Adv Mar. 2024;10(9):6501. https://doi.org/10.1126/sciadv.adk6501.

[43] Pikuda O, Garlisi C, Scandura G, Palmisano G. Micro-mesoporous N-doped brookite-rutile TiO2 as efficient catalysts for water remediation under UV-free visible LED radiation. J Catal 2017;346:109–16. https://doi.org/10.1016/j.jcat.2016.12.010.

[44] E. M. Abdelsalam, & Yasser, M. A. Mohamed, S. Abdelkhalik, H. A. El Nazer, and A. Attia, “Photocatalytic oxidation of nitrogen oxides (NO x) using Ag-and Pt-doped TiO 2 nanoparticles under visible light irradiation”, doi: 10.1007/s11356-020-09649-5/Published.

[45] Zhou R, et al. Continuous synthesis of Ag/TiO2 nanoparticles with enhanced photocatalytic activity by pulsed laser ablation. J Nanomater 2017;2017. https://doi.org/10.1155/2017/4604159.

[46] Dong B, He BL, Huang J, Gao GY, Yang Z, Li HL. High dispersion and electrocatalytic activity of Pd/titanium dioxide nanotubes catalysts for hydrazine oxidation. J Power Sources Jan. 2008;175(1):266–71. https://doi.org/10.1016/j.jpowsour.2007.08.090.

[47] Ibrahim NS, Leaw WL, Mohamad D, Alias SH, Nur H. A critical review of metal-doped TiO2 and its structure–physical properties–photocatalytic activity relationship in hydrogen production. Elsevier Ltd.; Oct. 30, 2020. https://doi.org/10.1016/j.ijhydene.2020.07.233.

[48] Moongraksathum B, Shang JY, Chen YW. Photocatalytic antibacterial effectiveness of Cu-doped TiO2 thin film prepared via the peroxo sol-gel method. Catalysts Sep. 2018;8(9). https://doi.org/10.3390/catal8090352.

[49] Chen H, Liu G, Wang L. Switched photocurrent direction in Au/TiO2 bilayer thin films. Sci Rep 2015;5(Jun). https://doi.org/10.1038/srep10852.

[50] Li Y, et al. Solution-plasma-induced oxygen vacancy enhances MoOx/Pt electrocatalytic counter electrode for bifacial dye-sensitized solar cells. Front Energy Res 2022;10(Aug). https://doi.org/10.3389/fenrg.2022.924515.

[51] Yuan X, et al. Ti3+-Promoted high oxygen-reduction activity of Pd nanodots supported by black titania nanobelts. ACS Appl Mater Interfaces Oct. 2016;8(41): 27654–60. https://doi.org/10.1021/acsami.6b07062.

[52] Zhang M, Jin Z, Zhang Z, Dang H. Study of strong interaction between Pt and TiO 2 under oxidizing atmosphere. Appl Surf Sci Aug. 2005;250(1–4):29–34. https://doi.org/10.1016/j.apsusc.2004.12.032.

[53] Chen Y, et al. Facet-engineered TiO2 drives photocatalytic activity and stability of supported noble metal clusters during H2 evolution. Nat Commun Dec. 2023;14 (1). https://doi.org/10.1038/s41467-023-41976-2.

[54] Mukri BD, Waghmare UV, Hegde MS. Platinum ion-doped TiO2: high catalytic activity of Pt 2+ with oxide ion vacancy in Ti4+1-xPt 2+xO2- x compared to Pt4+ without oxide ion vacancy in Ti4+1-xPt4+xO2. Chem Mater Oct. 2013;25(19): 3822–33. https://doi.org/10.1021/cm4015404.

[55] Kato S, Suzuki S, Ogasawara M. Synthesis and reversible oxidation/reduction behavior of delafossite-type CuCr1−xAlxO2. J Mater Sci Sep. 2017;52(18): 10718–25. https://doi.org/10.1007/s10853-017-1263-7.

[56] Hou E, et al. Preparation of Ag–TiO2/MXene composite material for electrochemical detection of paraquat. J Mater Sci Mater Electron May 2023;34 (14). https://doi.org/10.1007/s10854-023-10603-7.

[57] López Ortiz A, Meléndez Zaragoza M, Salinas Gutiérrez J, Marques Da Silva Paula M, Collins-Martínez V. Silver oxidation state effect on the photocatalytic properties of Ag doped TiO2 for hydrogen production under visible light. In: International journal of hydrogen energy. Elsevier Ltd; Dec. 2015. p. 17308–15. https://doi.org/10.1016/j.ijhydene.2015.09.058.

[58] Muraoka M, et al. CO oxidation at low temperatures over the Au cluster supported on crystalline silicotitanate. ACS Omega Oct. 2024. https://doi.org/10.1021/acsomega.4c05778.

[59] Siavash Moakhar R, et al. AuPd bimetallic nanoparticle decorated TiO2 rutile nanorod arrays for enhanced photoelectrochemical water splitting. J Appl Electrochem Sep. 2018;48(9):995–1007. https://doi.org/10.1007/s10800-018-1231-1.

[60] Scandura G, Rodríguez J, Palmisano G. Hydrogen and propane production from butyric acid photoreforming over Pt-TiO2. Front Chem Aug. 2019;7. https://doi.org/10.3389/fchem.2019.00563.

[61] Roy N, Bhunia K, Terashima C, Fujishima A, Pradhan D. Citrate-capped hybrid Au-TiO2 nanomaterial for facile and enhanced electrochemical hydrazine oxidation. ACS Omega Mar. 2017;2(3):1215–21. https://doi.org/10.1021/acsomega.6b00566.

[62] Skalska K, et al. NOx photooxidation over different noble metals modified TiO2. Catalysts Aug. 2022;12(8). https://doi.org/10.3390/catal12080857.

[63] Çakír D, Gülseren O. Adsorption of Pt and bimetallic PtAu clusters on the partially reduced rutile (110) TiO 2 surface: a first-principles study. J Phys Chem C Mar. 2012;116(9):5735–46. https://doi.org/10.1021/jp2109253.

[64] Zhou Y, Muhich CL, Neltner BT, Weimer AW, Musgrave CB. Growth of Pt particles on the anatase TiO 2 (101) surface. J Phys Chem C Jun. 2012;116(22):12114–23. https://doi.org/10.1021/jp302273m.

[65] Han Y, Liu CJ, Ge Q. Interaction of Pt clusters with the anatase TiO2(101) surface: a first principles study. J Phys Chem B Apr. 2006;110(14):7463–72. https://doi.org/10.1021/JP0608574.

[66] Han Y, Liu CJ, Ge Q. Effect of surface oxygen vacancy on Pt cluster adsorption and growth on the defective anatase TiO 2(101) surface. J Phys Chem C Nov. 2007;111 (44):16397–404. https://doi.org/10.1021/jp075602k.

[67] Feng H, Zhang MH, Yu LE. Hydrothermal synthesis and photocatalytic performance of metal-ions doped TiO 2. Appl Catal Gen Jan. 2012;413–414: 238–44. https://doi.org/10.1016/j.apcata.2011.11.014.

[68] Alothman ZA. A review: fundamental aspects of silicate mesoporous materials. 2012. https://doi.org/10.3390/ma5122874.

[69] Ahmadiasl R, Moussavi G, Shekoohiyan S, Razavian F. Synthesis of Cu-doped TiO2 nanocatalyst for the enhanced photocatalytic degradation and mineralization of gabapentin under UVA/LED irradiation: characterization and photocatalytic activity. Catalysts Nov. 2022;12(11). https://doi.org/10.3390/catal12111310.

[70] Grabowska E, et al. Modification of titanium(IV) dioxide with small silver nanoparticles: application in photocatalysis. J Phys Chem C Jan. 2013;117(4): 1955–62. https://doi.org/10.1021/jp3112183.

[71] Fan X, et al. Preparation and characterization of Ag deposited and Fe doped TiO2 nanotube arrays for photocatalytic hydrogen production by water splitting. Ceram Int Dec. 2014;40(10):15907–17. https://doi.org/10.1016/j.ceramint.2014.07.119.

[72] Sellappan R, Nielsen MG, González-Posada F, Vesborg PCK, Chorkendorff I, Chakarov D. Effects of plasmon excitation on photocatalytic activity of Ag/TiO 2 and Au/TiO2 nanocomposites. J Catal 2013;307:214–21. https://doi.org/10.1016/j.jcat.2013.07.024.

[73] Ghosh SK, Nath S, Kundu S, Esumi K, Pal T. Solvent and ligand effects on the localized surface plasmon resonance (LSPR) of gold colloids. J Phys Chem B Sep. 2004;108(37):13963–71. https://doi.org/10.1021/jp047021q.

[74] Chen Y, Soler L, Armengol-Profitós M, Xie C, Crespo D, Llorca J. Enhanced photoproduction of hydrogen on Pd/TiO2 prepared by mechanochemistry. Appl Catal, B 2022;309(Jul). https://doi.org/10.1016/j.apcatb.2022.121275.

[75] Krishnakumar V, Boobas S, Jayaprakash J, Rajaboopathi M, Han B, Louhi-Kultanen M. Effect of Cu doping on TiO2 nanoparticles and its photocatalytic activity under visible light. J Mater Sci Mater Electron Jul. 2016;27(7):7438–47. https://doi.org/10.1007/s10854-016-4720-1.

[76] Bumajdad A, Madkour M. Understanding the superior photocatalytic activity of noble metals modified titania under UV and visible light irradiation. Royal Society of Chemistry; Apr. 28, 2014. https://doi.org/10.1039/c3cp54411g.

[77] Nabil S, Hammad AS, El-Bery HM, Shalaby EA, El-Shazly AH. The CO2 photoconversion over reduced graphene oxide based on Ag/TiO 2 photocatalyst in

an advanced meso-scale continuous-flow photochemical reactor 2021;28: 36157–73. https://doi.org/10.1007/s11356-021-13090-7.

[78] Fakhrutdinova E, Reutova O, Maliy L, Kharlamova T, Vodyankina O, Svetlichnyi V. Laser-based synthesis of TiO2-Pt photocatalysts for hydrogen generation. Materials Nov. 2022;15(21). https://doi.org/10.3390/ma15217413.

[79] Ângelo J, Magalhães P, Andrade L, Mendes A. Characterization of TiO2 -based semiconductors for photocatalysis by electrochemical impedance spectroscopy. Appl Surf Sci Nov. 2016;387:183–9. https://doi.org/10.1016/j.apsusc.2016.06.101.

[80] Pan Y, Wen M. Noble metals enhanced catalytic activity of anatase TiO2 for hydrogen evolution reaction. Int J Hydrogen Energy Dec. 2018;43(49):22055–63. https://doi.org/10.1016/j.ijhydene.2018.10.093.

[81] Yang H, Yang B, Chen W, Yang J. Preparation and photocatalytic activities of TiO2-based composite catalysts. MDPI; Oct. 01, 2022. https://doi.org/10.3390/catal12101263.

[82] Schneider J, et al. Understanding TiO2photocatalysis: mechanisms and materials. Am Chem Soc Oct. 08, 2014. https://doi.org/10.1021/cr5001892.

[83] Wrana D, et al. Photoluminescence imaging of defects in TiO2: the influence of grain boundaries and doping on charge carrier dynamics. Appl Surf Sci Dec. 2021; 569. https://doi.org/10.1016/j.apsusc.2021.150909.

[84] Medford AJ, et al. From the Sabatier principle to a predictive theory of transition-metal heterogeneous catalysis. J Catal Jul. 2015;328:36–42. https://doi.org/10.1016/J.JCAT.2014.12.033.